ACSNANO
www.acsnano.org
ARTICLE

Far-Field Super-resolution Detection of Plasmonic Near-Fields

Robert Charles Boutelle,[†] Daniel Neuhauser,*[,†,‡] and Shimon Weiss*[,†,‡,§,∥]

[†]Department of Chemistry & Biochemistry, [‡]California NanoSystems Institute, and [§]Department of Physiology, University of California Los Angeles, Los Angeles, California 90095, United States

[∥]Department of Physics, Bar Ilan University, Ramat Gan, 52900, Israel

Supporting Information

ABSTRACT: We demonstrate a far-field single molecule super-resolution method that maps plasmonic near-fields. The method is largely invariant to fluorescence quenching (arising from probe proximity to a metal), has reduced point-spread-function distortion compared to fluorescent dyes (arising from strong coupling to nanoscopic metallic features), and has a large dynamic range (of 2 orders of magnitude) allowing mapping of plasmonic field-enhancements regions. The method takes advantage of the sensitivity of quantum dot (QD) stochastic blinking to plasmonic near-fields. The modulation of the blinking characteristics thus provides an indirect measure of the local field strength. Since QD blinking can be monitored in the far-field, the method can measure localized plasmonic near-fields at high throughput using a simple far-field optical setup. Using this method, propagation lengths and penetration depths were mapped-out for silver nanowires of different diameters and for different dielectric environments, with a spatial accuracy of ∼15 nm. We initially use sparse sampling to ensure single molecule localization for accurate characterization of the plasmonic near-field with plans to increase density of emitters in further studies. The measured propagation lengths and penetration depths values agree well with Maxwell finite-difference time-domain calculations and with published literature values. This method offers advantages such as low cost, high throughput, and superresolved mapping of localized plasmonic fields at high sensitivity and fidelity.

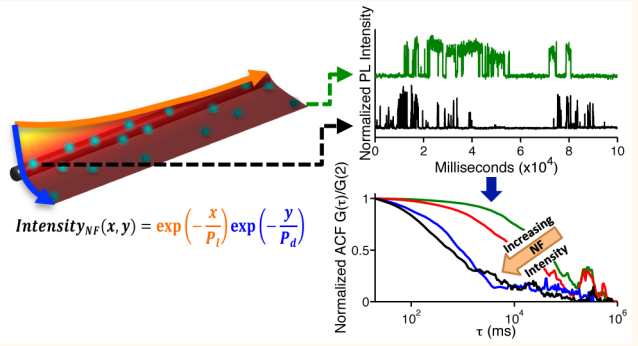

KEYWORDS: *super-resolution, near-field, quantum dot, blinking, plasmonics, far-field*

Surface plasmon polaritons (SPP), the coupling of photons to charges at metal interfaces, improves the efficiency of sensing,[1,2] energy transfer,[3−5] and catalysis.[6] There has been much effort to optimize plasmonic systems and exploit their field enhancement property. However, the system structure, resonance frequencies, and field enhancement are all coupled, making characterization difficult.[7] Thus, with the development of plasmonics-based devices and circuits there is a growing need for detecting and characterizing plasmonic effects in large systems. While Maxwell finite-domain time-difference (FDTD) simulations can handle ideal systems, measurement and characterization of realistic (imperfect) experimental systems is desired. The common approach for measuring plasmonic fields is near-field scanning optical microscope (NSOM),[8−10] which is slow due to a feedback loop. Alternatives, such as two-photon luminescence imaging,[11] electron energy loss spectroscopy,[12,13] photoemission electron microscopy,[14] cathode-luminescence spectroscopy,[15] and bleach-image plasmon propagation (BlIPP),[4,7,16] are still diffraction limited, costly, or have low throughput.

Single-molecule super-resolution methods, such as PALM and STORM, have better resolution than conventional optical microscopy.[17−19] The simplest super-resolution approach for measuring plasmonic fields uses a polymer layer doped with fluorescent molecules close to a planar metal layer.[20−22] Such emitters could be localized at high precision and their emission intensity should be measured (assuming that it is proportional to the plasmonic excitation field). However, characterization of plasmonic near-fields using an emitter's fluorescent intensity has many complications. Fluorescence enhancement and quenching effects cause the fluorescence intensity to vary non-monotonically as a function of the probe distance less than 30 nm from the metal.[20,23] Additionally, the point-spread function (PSF) of an emitter placed within 100 nm of a metallic surface is distorted due to strong electromagnetic coupling of the emitter's dipole to the nearby metallic structure. The

Received: June 12, 2016
Accepted: August 8, 2016
Published: August 8, 2016

DOI: 10.1021/acsnano.6b03873
ACS Nano 2016, 10, 7955−7962

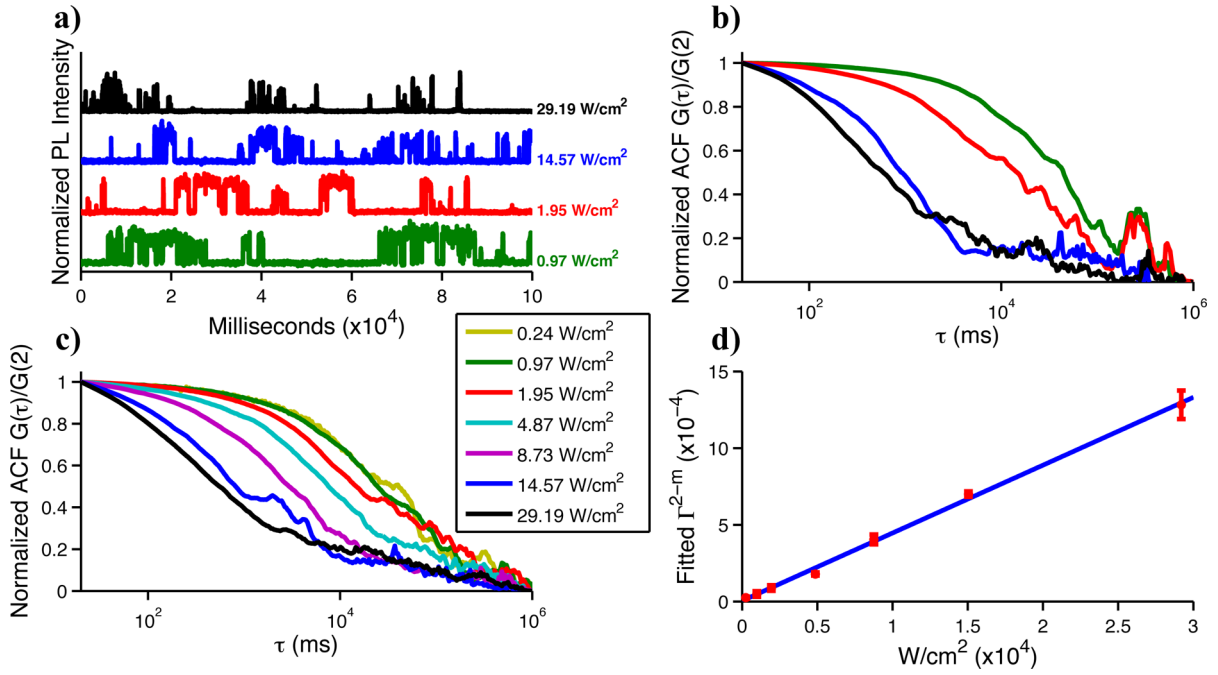

Figure 1. QD excitation intensity sensitivity. (a) Typical intensity trajectories of a single QD under a 642 nm CW laser excitation for varying excitation powers. (b) Corresponding normalized ACFs of a single QD at different excitation powers. (c) Averaged normalized ACFs from 30 individual QDs at various excitation powers. A clear trend of a faster decaying ACF is seen at higher powers due to shorter "on" lifetimes. (d) Plot and a fit to Γ^{2-m} as a function of excitation power density (according to eq 2). The results show a clear linear trend within the tested dynamic range of power densities. The fitting yields $\Gamma^{2-m} = 4.4 \times 10^{-8}$ cm^2 W^{-1} s$^{-1} \times P + 4.3 \times 10^{-6}$ s^{-1}, where P is excitation power in W/cm^2.

superposition of scattered light PSF from the metal surface and dipole emitter PSF causes an erroneous localization of the far-field PSF away from the true location of the probe.[24−27] When within several nanometers of a metallic structure, a distance of particular interests for nanoparticle plasmonics, the underlying structure can completely distort an emitter's PSF to non-Gaussian shapes, making localization difficult without knowing the underlying structure.[25] Lastly, the relation between excitation and emission is nonlinear at strong fields due to saturation.

Here, stochastic quantum dot (QD) blinking[28−31] is proposed and demonstrated as an approach for sensing plasmonic near-fields. Previous studies have already demonstrated that QD blinking is relatively invariant to enhancement and quenching effects.[32] Additionally, spherical QDs have a degenerate in-plane dipole and therefore weaker electromagnetic coupling to metallic antenna structures.[27,33,34] The weaker coupling creates less distortion in the QD PSF and should allow more accurate localization compared to a conventional fluorescent dye.[27] Using these attributes, we show that blinking QDs are good reporters of plasmonic (near) field strength. Moreover, QDs' blinking can be monitored using wide-field, far-field optics at high throughput and high localization accuracy.

A direct demonstration of the spatial and field intensity sensitivity of blinking QD reporters is done here on silver nanowires (Ag NWs). Ag NW waveguides have an inhomogeneous (decaying) field distribution both in the SPP propagation direction (along the long direction of the wire) and penetration depth direction (perpendicular to the long direction of the wire).[35] QDs were spin-coated on top of Ag NWs having different dimensions and dielectric environments. The wires were overcoated with either of two different types of dielectric layers: SiO_2 or poly(methyl methacrylate) (PMMA). The wires were then sparsely labeled with QDs ~30 nm from the Ag NW surface to ensure accurate single molecule localization and extraction of the plasmonic near-field strength. These experiments allowed us to test the dependence of the SPP propagation decay length and penetration depth on the wire diameter and on the environment's dielectric constant. The fitted experimental results for propagation length and penetration depth were favorably compared to FDTD simulations and to values reported in the published literature.

RESULTS AND DISCUSSION

Field Intensity Sensitivity of QDs. Optical field intensities affect the stochastic switching of QDs between an "on" state with a high photon emission rate and an "off" low emission state. Stochastic switching, also known as "intermittency", or "blinking",[28−31] has been studied extensively, both experimentally and theoretically.[28,31,36−38] Auger recombination is commonly invoked to explain blinking,[39−41] but other processes, such as surface and heterointerface charge trapping, have also been shown to contribute to the switching.[42,43] Auger recombination is a three-particle process that results in a nonradiative transition due to the absorption of energy from an exciton by a spectator particle, leaving the QD charged, and in a "dark", or "off", state. Only once the charged QD is neutralized does the emissive "on" state resume.

Blinking in QDs is inherently stochastic and independent of other nearby QD emitters. Traditionally, emission from a single QD is recorded in time bins to analyze the blinking phenomena. A threshold is used to discern "on" and "off" time periods in the telegraph noise-like time trajectory and histograms are constructed for the "on" and "off" periods. At low excitation power, the histograms exhibit a near perfect

DOI: 10.1021/acsnano.6b03873
ACS Nano 2016, 10, 7955−7962

power law distribution for both the "on (+)" and "off (−)" states, described by $P_{\pm}(t) = t^{-m}$. For higher excitation energies, the "on" time distribution starts to bend at long "on" times ($P_{+} = t^{-m}e^{-\Gamma t}$ where Γ is the intensity bending parameter).[28−31] Here, m is the slope of the on/off-time probability distribution in a log−log plot. Thus, the stronger the excitation intensity, the shorter the "on" periods and the more likely the QD will be to enter an "off" state. The bending parameter, Γ, yields information on the excitation field *via* the blinking statistics of individual QDs.

To further establish the relationship between Γ and the excitation field strength, blinking experiments were performed similarly to previously published works. However, since typical analysis of on/off time histograms can lead to a 15−30% bias in extraction of parameters (depending on background noise and binning of photons[38]), we instead utilized autocorrelation functions (ACFs) for the analysis. ACFs are mostly insensitive to binning and thresholding artifacts and therefore provide a more reliable and robust analysis.[44,45] The bending parameter Γ was analyzed as a function of increased excitation intensity. Following the work of Verberk and Orrit,[46] the Laplace transform of the normalized ACF can be written as

$$g(s) = \frac{1}{s}\left[1 - \frac{1}{sT_{+}} \times \frac{(1 - p_{+})(1 - p_{-})}{1 - p_{+}p_{-}}\right] \quad (1)$$

where $p_{+}(s)$ and $p_{-}(s)$ are the Laplace transforms of the on/off-time probability distributions, $p_{+}(t) \propto t^{-m}e^{-\Gamma t}$ and $p_{-}(t) \propto t^{-m}$, respectively, and T_{+} is the average on-time. Simplifying with the assumption that the minimum capture window will be much smaller than the total time trajectory collected, such that $s \to 0$, and transforming back with an inverse Laplace transform, we obtain

$$1 - G(\tau) = \beta(m)\theta^{m-1}\Gamma^{2-m}\tau^{2-m} \quad (2)$$

where θ is the minimum capture window and $\beta(m)$ is a numerical function (product of Γ-functions) of m. The parameter θ is known from the experimental minimum capture time (10 ms in our case). A full derivation of eq 2 is given in the Supporting Information.

Benchmark studies of Γ as a function of excitation power were performed on 30 individual CdSe/ZnS core−shell QDs with emission centered at 800 nm. Figure 1a shows typical intensity trajectories from a single CdSe/ZnS core−shell QDs at different excitation powers, excited at 642 nm with a continuous wave (CW) laser (Coherent, Wilsonville, OR). The 800 nm emission from the QDs was filtered from the excitation wavelength using a 750 nm long band-pass filter (ThorLabs, Newton, NJ) and intensity measured in wide-field with an EMCCD camera (Andor, Waltham, MA). As the excitation power increases, the normalized ACF decays more rapidly due to shortened "on" times (Figure 1b). For a single QD, the autocorrelation function at different excitation powers was fit to eq 2, keeping m a global variable between excitation power and Γ a local variable. This procedure was repeated for all 30 QDs (average ACFs in Figure 1c). The resulting fit of m for each QD gives $m = 1.40 \pm 0.03$, in good agreement with previously reported values of $m \approx 1.5 \pm 0.2$.[36] When the intensity parameter Γ was fit as a function of excitation power, a linear trend is observed over 2 orders of magnitude of intensity. When the data is fit we obtain a direct relationship between Γ^{2-m} and excitation power

$$\Gamma^{2-m} = 4.4 \times 10^{-8}\ \text{cm}^2\ \text{W}^{-1}\ \text{s}^{-1} \times P + 4.3 \times 10^{-6}\ \text{s}^{-1} \quad (3)$$

where P is excitation power (W/cm^2) (Figure 1d). These results follow a trend similar to previously reported values extracted using different analysis methods.[44,47] Figure 1 therefore represents a calibration method for determining the excitation intensity from the blinking behavior of individual QDs. We dub this approach COFIBINS (**C**haracterizing **O**ptical **F**ield **I**ntensity by **Bl**Inking **N**anoparticle**S**).

Extracting the Plasmonic Field Intensity by Localized Blinking QDs. A direct application of COFIBINS to the characterization of plasmonic waveguide (*i.e.*, extraction of propagation length and penetration depth) by localized blinking QDs is demonstrated next.

Three different NW waveguides with mean diameters of 160, 290, and 400 nm were prepared in order to test the variation of SPP propagation lengths and penetration depths as a function of the Ag NW diameter. Additionally, the Ag NWs were overcoated with either a 30 nm thick SiO_2 layer or a 30 nm thick PMMA layer in order to compare differences in propagation lengths and penetration depths as a function of the refractive index of the two environments. The prepared system dimensions are shown in Figure 2. Additional experimental details are given in the SI.

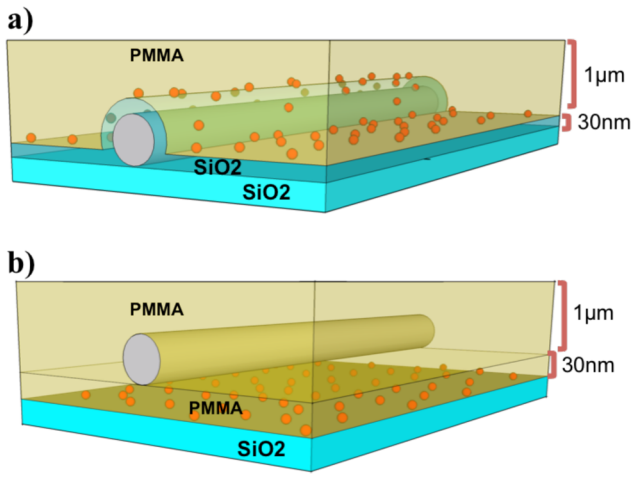

Figure 2. Samples structures and dimensions of silver nanowire surrounded by (a) silicon dioxide and (b) PMMA. Notice that QDs (red dots) are at the SiO_2−PMMA interface for both samples.

The dielectric dependence studies were designed to create two different dielectric environments for the Ag NWs (SiO_2 or PMMA) while keeping QDs in a constant environment (PMMA−SiO_2 interface, see Figure 2) since QD blinking has been shown to be sensitive to the immediate dielectric environment.[47] The QDs were spin-coated with an areal density of ∼1.8 QDs/μm^2 (to ensure single particle localization conditions). Upon localized excitation at one end of the silver nanowire, the plasmonic field intensity exponentially decays along (and perpendicular to) the wire. The 2-D mapping of the plasmonic field is accomplished by localizing each QD PSF centroid relative to the Ag NW and extracting the local field intensities of each QD from their blinking time intensity trajectories. Figure 3b shows a single frame from a movie that recorded the emission from QDs dispersed over the SPP waveguide. The location of each QD was localized (by 2D Gaussian fitting) with a spatial accuracy of ∼15 nm. Accuracy

DOI: 10.1021/acsnano.6b03873
ACS Nano 2016, 10, 7955−7962

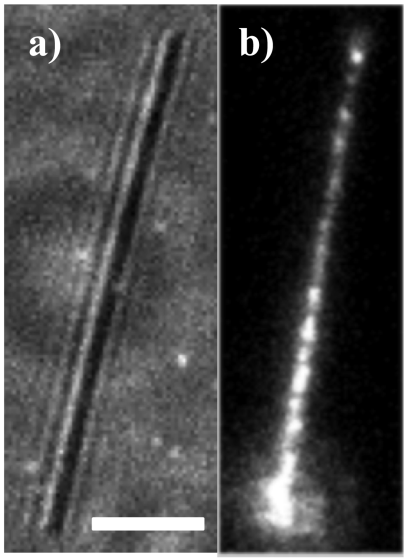

Figure 3. SPP propagation image. Silver nanowire with dimensions 0.2 μm × 20 μm (a) under bright field illumination and (b) wide-field fluorescence image of blinking QDs on top of the wire. A diffraction-limited focused laser excitation excites the silver wire at the bottom end of the silver wire. The plasmon propagation is visualized by the evanescent field exciting the QDs on the wire. Scale bar is 4 μm.

was determined from fitting experimental data with a known background plus the calculated error due to the dipole-SPP coupling as modeled below (see the Supporting Information for more details). The calculated error in localization is represented by the error bars in Figure 4b,c.

The physical location of the metal wire relative to the QD was determined by drawing a straight line between two Gaussian fits to the scattered light emanating at the downstream end of the wire, as the SPP were alternatively excited at each end (see SI Figure 2 for more details). The extracted radial distance (perpendicular to the long axis of the wire's center), longitudinal distance from the wire's end, and intensity dependent Γ factor were then extracted for each QD. The origin of the 2D plane is defined as the locally excited Ag NW end found by fitting a 2D Gaussian to scattered light at the end. We define the x-axis as the propagating field along the long axis of the wire and y-axis as the field penetration into the local media orthogonal to the Ag NW. For simplicity, the y-axis was mirrored such that $y = -y$. Figure 4 plots the near-field intensity extracted from the Γ value of each QD, using eq 3, and plotted against the fitted x and y PSF location. The near-field intensity data was broken into two groups to make the data more palatable: propagation length and penetration depth. The extracted normalized QD intensity data was initially fit to the function $I(x, y) = N \times \exp(-x/P_l) \times \exp(-y/P_d)$, where N is the amplitude, P_l is the SPP propagation length, P_d is the SPP penetration depth, x is the distance along the wire, and y is the distance perpendicular to the wire. The fit values of P_l and P_d are then graphed in Figure 4b,c as $I(x)/N = \exp(-x/P_l)$ and $I(y)/N = \exp(-y/P_d)$, respectively. The extracted normalized individual QDs intensities are separated into propagation length and penetration depth plots as $I(x) = I(x, y)/N \exp(-y/P_d)$ and $I(y) = I(x, y)/N \exp(-x/P_l)$, illustrating QD's sensitivity to position along, and perpendicular to, the Ag NW. The exponential decays along, and perpendicular to, the Ag NW are evident. We measured eight individual Ag NWs for each combination of dielectric environment (SiO_2 and PMMA) and Ag NW diameters (160, 290, and 400 nm) for a total of 48

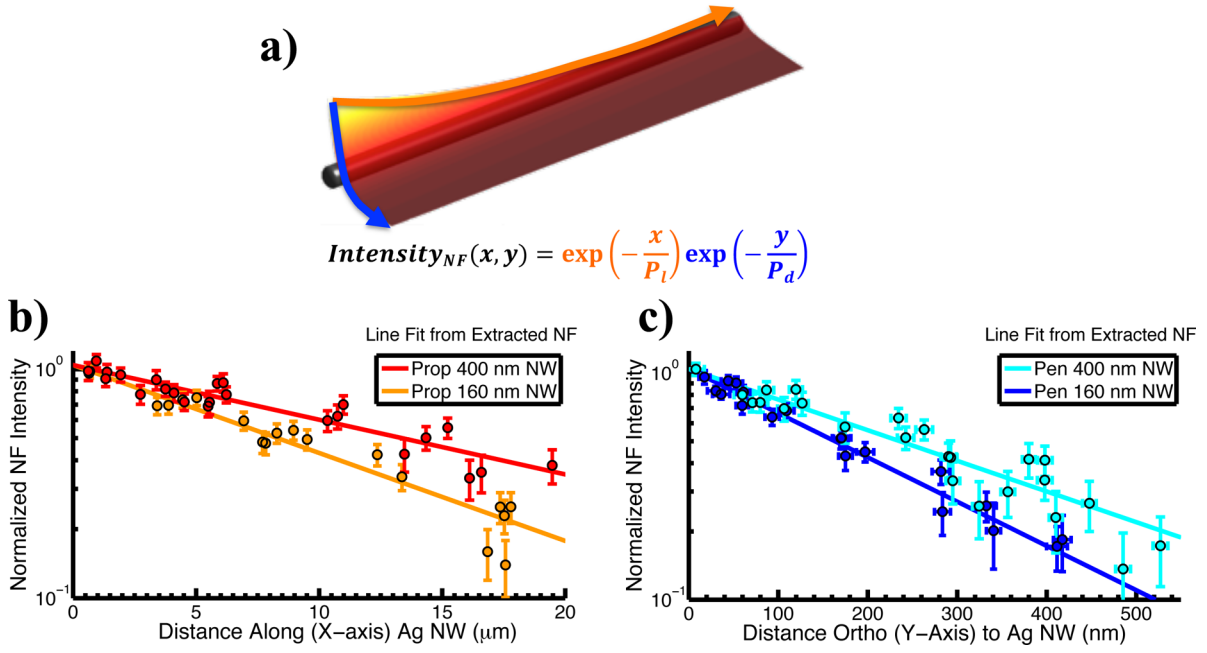

Figure 4. Near-field intensity as a function of QD position. (a) Near-field intensity as a function of distance from excitation point along an Ag NW. (b, c) Extracted near-field intensity (normalized) values from ~20 QDs as a function of their x, y fitted coordinates on a 160 and 400 nm Ag NW in PMMA. To illustrate the propagation length and penetration depth, the extracted normalized individual QDs intensities are separated and plotted as $I(x) = I(x, y)/N \exp(-y/P_d)$ and $I(y) = I(x, y)/N \exp(-x/P_i)$ for (b) and (c), respectively. From these fits, SPP propagation length and penetration depth are determined. The x-error bars are from calculated error in PSF fitting. The y-error is determined from uncertainties in our calibration curve (Figure 1c). The data point size in (b) is larger than the x-error and thus omitted.

DOI: 10.1021/acsnano.6b03873
ACS Nano 2016, 10, 7955−7962

Table 1. Experimentally Extracted Values and Theoretical Values for Penetration Depths and Propagation Lengths of Different Diameter NWs Embedded in Different Dielectric Environments (PMMA or SiO_2)

		160 nm Ag NW		290 nm Ag NW		400 nm Ag NW	
dielectric		propagation (μm)	penetration (nm)	propagation (μm)	penetration (nm)	propagation (μm)	penetration (nm)
PMMA	experiment	11.02 ± 0.81	254.8 ± 11.30	15.03 ± 1.90	275.68 ± 24.30	18.59 ± 1.90	306.87 ± 17.08
	theory	10.37 ± 1.20	252.72 ± 3.15	15.19 ± 0.93	270.45 ± 4.45	17.39 ± 1.07	286.07 ± 8.26
SiO_2	experiment	11.92 ± 2.13	198.09 ± 33.48	15.66 ± 0.95	210.74 ± 36.69	20.35 ± 2.78	216.05 ± 49.15
	theory	11.98 ± 0.89	200 ± 0.29	15.94 ± 0.83	201 ± 0.35	18.01 ± 1.04	203 ± 0.42

samples. The extracted SPP propagation length and penetration depth are compared to theoretical FDTD predictions in Table 1 and Figure 5.

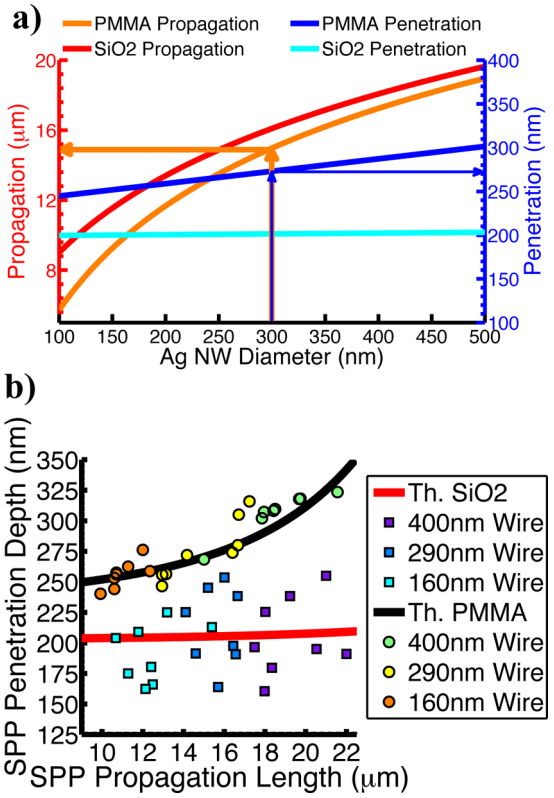

Figure 5. Theoretical and experimental near-field intensity. (a) Theoretical calculations of propagation lengths (left *y*-axis) and penetration depths (right *y*-axis) as a function of the nanowire diameter. The arrows (orange and blue) give an example for reading the penetration depth and propagation length for a 300 nm Ag NW covered in PMMA. The change in PMMA penetration depth as a function of NW radius is explained in the SI (and SI Figure 4). (b) Comparison of experimental and theoretical penetration depth *vs* propagation length values for various wire diameters. The distribution of measured Ag NWs in SiO_2 (square) and PMMA (circle) compare favorably to the theoretical expected values (black and red lines). Additionally, the different-sized Ag NWs group together and show the expected trend of increased SPP propagation length and penetration depth for larger wire diameters.

Comparing Analytical and FDTD Predictions. Ag NW waveguides were modeled using the FDTD method. Simulation parameters matched the experiments. Experimentally determined NW diameters (SI Figure 2) and literature values for SiO_2 (n = 1.542) and PMMA (n = 1.488) refractive indexes were used. For the complex dielectric function of Ag, the tabulated values by Johnson and Christy were used.[48] The complex refractive index used in simulations was fit using nine drude oscillators derived in a previous work.[49] Ag NW waveguides were excited in the simulation at one end with a focused 642 nm CW laser beam (with a PSF of 321 nm fwhm) at the wire's end. See the SI for detailed information on the simulations. Figure 5 shows the theoretical dependencies of the propagation length and penetration depth parameters on the wire diameter and on the surrounding refractive index. Oddly, the PMMA sample penetration depth increases as a function of nanowire diameter. This result is due to the geometry of our sample and is explained in detail in the SI (and SI Figure 4).

The predicted mean and standard deviation of the SPP propagation length and penetration depth were calculated by applying the measured diameter distributions of the Ag NWs (SI Figure 1) to the theoretical diameter dependent propagation/penetration depth functions (Figure 5a). Overall, experimentally derived values and theory-derived values agree quite well, as noted in Table 1 and Figure 5. The deviation between theory and experiment is greater for larger wire diameters due to the pentagonal cross-section of the thicker experimental wires *vs* the circular wires used in the simulations. Additionally, the spread in SiO_2 penetration depth measurements was due to nonideality of our sample. The SiO_2 was deposited by vapor deposition leading to surface roughness and thickness variations, as well as oxidation of the Ag NWs' surfaces. Regardless, the experimental data show close agreement to theoretical results.

The experiments clearly demonstrate an increase in SPP propagation length for larger wire diameters and for larger refractive index of the surrounding. They also demonstrate an increase in the penetration depth as a function of the NW diameter. This latter observation is attributed to the geometries of our samples, as explained in detail in SI Figure 4. The larger diameter wire could act as a larger antenna that radiates further into the local environment.

FDTD calculations were used to estimate the error in localizing the QD (dipole) emitters when in close proximity to NWs. Due to antenna effects, the QD's far-field emission is a superposition of its direct emission plus it scattering off the wire antenna (its mirror charge dipole on the metal surface also radiates into the far-field). The superposition of the direct dipole emission with the scattering from the metallic wire leads to an erroneous PSF localization in the far field. Near-field to far-field scattering simulations were conducted to determine the strength of the electromagnetic coupling of a dipole to a wire antenna, and localization errors were quantified (SI Figure 5). The near-field to far-field conversion is similar to that used for determining radar cross sections.[50] The errors associated with this scattering effect were added into the overall localization error bars of Figure 4. (See the SI for more details.)

Interestingly, our calculated localization error for a QD placed near an Ag NW is smaller than the error calculated (and

DOI: 10.1021/acsnano.6b03873
ACS Nano 2016, 10, 7955−7962

reported) for a linear dipole.[24] There are two possible reasons for this discrepancy. First, the long Ag NW (as compared to the metallic structures in ref 23) acts as a waveguide that propagates the coupled QD radiation away from the QD (and hence reduces the scattering component). Second, the in-plane degeneracy of the QD's emission dipole[33,34] can also reduce scattering (to be further studied in a future work).

CONCLUSIONS

We have characterized the dependence of QDs' stochastic blinking on optical field strength and have shown that the bending parameter Γ can be used to measure SPP field strength. This allowed us to study the dependencies of Ag NWs propagation length and penetration depth on wire diameter and refractive index of the wire's surroundings. FDTD simulations were used to compare theoretical propagation lengths and penetration depth with experimentally derived values. Our theoretical predictions correlate well with the experiments and with known literature values.

COFIBINS offers an exciting sensitive method for detecting plasmonic near-fields using far-field optics. Since QD blinking can be monitored in the far-field, the method enables the measurement of localized plasmonic near-fields at high throughput using a simple far-field optical setup. QD blinking statistics are largely invariant to enhancement and quenching effects, and QD localization errors are <15 nm. QDs blinking is therefore an attractive probe that could be utilized for the characterization of plasmonic circuits, nanocatalysts, and solar concentrators.

In future studies, we plan to further enhance the resolution of COFIBINS by utilizing polarization to partly decouple the QD dipole from the metallic structures. This will reduce the overall scattering component and will lead to an even higher localization accuracy. Additionally, to completely map the plasmonic near-field with this developed methods requires dense labeling with QD emitters. Super-resolution methods that already implement autocorrelation functions of QD emitters, such as SOFI, offer an exciting avenue to achieve this goal. In future studies, we plan to incorporate COFIBINS with SOFI to allow complete plasmonic near-field mapping with densely labeled QD plasmonic systems.

EXPERIMENTAL SECTION

Sample Preparation. First, Ag NWs were synthesized using a modified polyol method described previously[51] or bought. The NWs lengths and widths were determined by scanning electron microscopy. The Ag NWs were measured to have average dimensions of 30 ± 10 μm long with an average diameter of 160 ± 20 nm, 290 ± 30 nm, and 400 ± 50 nm, respectively (SI Figure 1).

The PMMA NW samples were created according to the following steps. (i) Coverslip slides were cleaned by washing with a series of solutions (1.0 M KOH, DI-water, ethanol, and acetone) followed by an oxygen plasma cleaning (PDC-32G, Harrick Plasma, Ithica, NY) for 5 min. (ii) Water-soluble CdSe/ZnS QDs were spin-coated in water onto the coverslips to ensure even coverage. The sample was then put on a 100 °C hot plate for 3 min to dry. (iii) A 1 wt % solution of poly(methyl methacrylate) (PMMA) in toluene (an orthogonal solvent to water) was spin-coated onto the QD-coated coverslip at 8000 rpm for 1 min to ensure a dry, even 30 nm coating of PMMA on the surface. The film thickness of PMMA polymer was measured by scratching the polymer film and imaging the scratch using profilometry (Dektak 150, Veeco, Edina, MN). Samples were further dried on a 100 °C hot plate for 3 min to ensure removal of solvent. (iv) Silver nanowires suspended in ethanol were then dried on a PDMS stamp and stamped onto the PMMA surface. Stamping (dry deposition) of the NWs ensures minimal disruption to the PMMA-covered QDs. (v) Finally, a 3 wt % solution of PMMA in toluene was spun at 3000 rpm to embed the silver NWs in a well-defined dielectric environment.

The SiO_2-covered NW samples were created according to the following steps: (i) coverslip slides were cleaned in the same fashion as above; (ii) Ag NWs suspended in ethanol were spin-coated at 3000 rpm for 1 min onto the cleaned coverslip surfaces; (iii) samples (in a container) were rapidly moved into the cleanroom, and a 30 nm layer of SiO_2 was deposited *via* electron beam evaporator (CHA solution, Freemont, CA); (iv) during SiO_2 deposition, water-soluble QDs were spin-coated onto a PDMS stamp and allowed to dry; (v) once SiO_2 deposition was completed, QDs were immediately stamped onto the SiO_2 surface. Stamping of QDs minimized disruptions and provided uniform QD coverage on the surface; (vi) finally, a 3 wt % solution of PMMA in toluene (an orthogonal solution to the water-soluble QDs) was spin-coated on the surface to provide the same environment for the QDs in both samples.

Optical Measurements. Optical measurements were acquired using a 642 nm continuous wave solid-state laser (Part No. 1150205/AD, Coherent, Wilsonville, OR) for excitation, an XY automated stage (MS-2000, Applied Scientific Instrumentation, Eugene, OR), an inverted microscope (Axiovert S100 TV, Zeiss, Thornwood, NY), a 100× magnification 1.4 NA objective (MPLAPON100XO, Olympus, Waltham, MA), and an EMCCD camera (Model No. DU-897E-CS0-#BV, Andor, Concord, MA). QD fluorescence (at 800 nm) was collected through a 750 nm long pass filter (ThorLabs Inc., Newton, NJ). Movies were recorded with the EMCCD camera. Integration time of 10 ms per frame and total acquisition time of 17 min (100000 frames) were used. Excitation power was determined at the back aperture of the objective using an optical power meter (Model No. 1830-C, Newport, Irvine, CA).

For the QD field intensity measurements, a lens was added before the side port of the microscope to expand the collimated laser and allow wide-field illumination of the sample. An iris was placed in front of the expanded beam to allow a known area size (625 μm^2) to be illuminated.

For SPP measurements on Ag NW, the laser was focused to a Gaussian spot (fwhm ∼500 nm) on one end of the wire. Laser PSF size was determined by focused laser excitation of high density labeled QDs on a glass coverslip and fitting the summed image of the QD emission on the EMCCD camera to a Gaussian. Power was reduced to a minimal level that still allowed QDs excitation (and detectable emission) at the far-end of the Ag NW (typically ∼100 W/cm^2).

FDTD Simulations. Electromagnetic simulations were carried out using the finite difference time domain (FDTD) method.[49] The surface plasmon polariton propagation was simulated on Ag NWs of length 20 μm and a diameter varying between 100 and 440 nm. The silver NWs were modeled as round cylinders with flat ends: cylindrical NW with a circular cross-section. This assumption is reasonable since the true pentagonal cross sections have corner modes that hybridize into a symmetric fundamental SPP mode that is similar to the $m = 0$ mode supported by a cylindrical NW. To model the PMMA-coated Ag NWs, the model considered an infinite large dielectric surface with refractive index of $n = 1.542$ for the glass coverslip followed by a 30 nm thick dielectric layer of infinite length and width with refractive index of $n = 1.488$ for the spin-coated layer of PMMA. The Ag NWs were positioned on top of this 30 nm PMMA layer. A final infinitely large dielectric layer with refractive index $n = 1.488$ fills in the rest of the modeled box, representing the final layer of PMMA on top of the Ag NW. Similar to the experiment, SPP excitation was done by a 642 nm focused laser beam with spatial fwhm of 321 nm exciting one end of the NW. For the complex dielectric function of Ag, drude oscillators were used, with response adjusted to the tabulated values of Johnson and Christy.[48] The emitted energy, which leaks from the NW into the surroundings, was analyzed in the plane where the QDs are experimentally: the plane at the SiO_2–PMMA interface, 30 nm below the Ag NW for this sample.

Similarly, to model the SiO_2-coated Ag NWs, again the model considered an infinite large dielectric surface with refractive index of $n = 1.542$ for the glass coverslip. However, the Ag NW is then directly

DOI: 10.1021/acsnano.6b03873
ACS Nano 2016, 10, 7955–7962

placed on the glass surface and a 30 nm thick dielectric layer with index of refraction n = 1.542, representing the deposited SiO_2, surrounds the Ag NW and coats the surface, similar to the experimental geometry. Finally, an infinitely large dielectric layer with refractive index n = 1.488 fills in the rest of the modeled box, representing the final layer of PMMA on top of the SiO_2-covered Ag NW. Again, the plane of the PMMA–SiO_2 interface is monitored. However, this plane is 30 nm above the coverslip, which lies tangent to the Ag NW surface.

Scattering effects were calculated using a near-field to far-field conversion *via* conventional radar cross-section methods.[50] These results were solely used to calculate the accuracy of localizing a QD near an Ag NW surface. The calculated error in localization is added as error bars to Figure 4. No corrections are made to the experimentally fit localization. See the SI for more information.

ASSOCIATED CONTENT

Supporting Information

The Supporting Information is available free of charge on the ACS Publications website at DOI: 10.1021/acsnano.6b03873.

Further details about sample preparation, optical measurements, ACF derivation, localization, and FDTD simulations (PDF)

AUTHOR INFORMATION

Corresponding Authors

*E-mail: dxn@ucla.edu.

*E-mail: sweiss@chem.ucla.edu.

Author Contributions

R.B., D.N., and S.W. designed the experiments. R.B. performed all experiments. R.B. and D.N. designed the simulations. R.B. performed simulations. R.B. analyzed the data. R.B., D.N., and S.W. wrote the paper. D.N. and S.W. initiated and managed the research project.

Notes

The authors declare no competing financial interest.

ACKNOWLEDGMENTS

We thank Xavier Michalet, Antonio Ingargiola, and Xiyu Yi for their feedback and discussions on stochastic quantum dot blinking statistics and how to accurately analyze the experimental data. This work was supported by the Dean Willard Chair Fund, NSF CHE-111250, and the U.S. Department of Energy Office of Science, Office of Biological and Environmental Research program under Award No. DE-FC02-02ER63421.

REFERENCES

(1) Elghanian, R.; Storhoff, J. J.; Mucic, R. C.; Letsinger, R. L.; Mirkin, C. A. Selective Colorimetric Detection of Polynucleotides Based on the Distance-Dependent Optical Properties of Gold Nanoparticles. *Science* **1997**, *277*, 1078–1081.

(2) Kneipp, K.; Wang, Y.; Kneipp, H.; Perelman, L. T.; Itzkan, I.; Dasari, R. R.; Feld, M. S. Single Molecule Detection Using Surface-Enhanced Raman Scattering (SERS). *Phys. Rev. Lett.* **1997**, *78*, 1667–1670.

(3) Barnes, W. L.; Dereux, A.; Ebbesen, T. W. Surface Plasmon Subwavelength Optics. *Nature* **2003**, *424*, 824–830.

(4) Solis, D.; Paul, A.; Olson, J.; Slaughter, L. S.; Swanglap, P.; Chang, W.-S.; Link, S. Turning the Corner: Efficient Energy Transfer in Bent Plasmonic Nanoparticle Chain Waveguides. *Nano Lett.* **2013**, *13*, 4779–4784.

(5) Paul, A.; Zhen, Y.-R.; Wang, Y.; Chang, W.-S.; Xia, Y.; Nordlander, P.; Link, S. Dye-Assisted Gain of Strongly Confined Surface Plasmon Polaritons in Silver Nanowires. *Nano Lett.* **2014**, *14*, 3628–3633.

(6) Christopher, P.; Xin, H.; Linic, S. Visible-Light-Enhanced Catalytic Oxidation Reactions on Plasmonic Silver Nanostructures. *Nat. Chem.* **2011**, *3*, 467–472.

(7) Nauert, S.; Paul, A.; Zhen, Y.-R.; Solis, D.; Vigderman, L.; Chang, W.-S.; Zubarev, E. R.; Nordlander, P.; Link, S. Influence of Cross Sectional Geometry on Surface Plasmon Polariton Propagation in Gold Nanowires. *ACS Nano* **2014**, *8*, 572–580.

(8) BETZIG, E.; TRAUTMAN, J. K.; HARRIS, T. D.; WEINER, J. S.; KOSTELAK, R. L. Breaking the Diffraction Barrier: Optical Microscopy on a Nanometric Scale. *Science* **1991**, *251*, 1468–1470.

(9) Onishi, S.; Matsuishi, K.; Oi, J.; Harada, T.; Kusaba, M.; Hirosawa, K.; Kannari, F. Spatiotemporal Control of Femtosecond Plasmon Using Plasmon Response Functions Measured by Near-Field Scanning Optical Microscopy (Nsom). *Opt. Express* **2013**, *21*, 26631–26641.

(10) Kim, J.; Song, K.-B. Recent Progress of Nano-Technology with NSOM. *Micron* **2007**, *38*, 409–426.

(11) Yashunin, D.; Ilin, N.; Stepanov, A.; Smirnov, A. Two-Photon Luminescence Imaging by Scanning Near-Field Optical Microscopy for Characterization of Gold Nanoparticles. *J. Phys. D: Appl. Phys.* **2014**, *47*, 305102.

(12) Bosman, M.; Keast, V. J.; Watanabe, M.; Maaroof, A. I.; Cortie, M. B. Mapping Surface Plasmons at the Nanometre Scale with an Electron Beam. *Nanotechnology* **2007**, *18*, 165505.

(13) Nelayah, J.; Kociak, M.; Stephan, O.; Garcia de Abajo, F. J.; Tence, M.; Henrard, L.; Taverna, D.; Pastoriza-Santos, I.; Liz-Marzan, L. M.; Colliex, C. Mapping Surface Plasmons on a Single Metallic Nanoparticle. *Nat. Phys.* **2007**, *3*, 348–353.

(14) Douillard, L.; Charra, F.; Korczak, Z.; Bachelot, R.; Kostcheev, S.; Lerondel, G.; Adam, P.-M.; Royer, P. Short Range Plasmon Resonators Probed by Photoemission Electron Microscopy. *Nano Lett.* **2008**, *8*, 935–940.

(15) Vesseur, E. J. R.; de Waele, R.; Kuttge, M.; Polman, A. Direct Observation of Plasmonic Modes in Au Nanowires Using High-Resolution Cathodoluminescence Spectroscopy. *Nano Lett.* **2007**, *7*, 2843–2846.

(16) Solis, D.; Chang, W.-S.; Khanal, B. P.; Bao, K.; Nordlander, P.; Zubarev, E. R.; Link, S. Bleach-Imaged Plasmon Propagation (BlIPP) in Single Gold Nanowires. *Nano Lett.* **2010**, *10*, 3482–3485.

(17) Betzig, E. Nobel Lecture: Single Molecules, Cells, and Super-Resolution Optics*. *Rev. Mod. Phys.* **2015**, *87*, 1153–1168.

(18) Moerner, W. E. Nobel Lecture: Single-Molecule Spectroscopy, Imaging, and Photocontrol: Foundations for Super-Resolution Microscopy*. *Rev. Mod. Phys.* **2015**, *87*, 1183–1212.

(19) Hell, S. W. Nobel Lecture: Nanoscopy with Freely Propagating Light*. *Rev. Mod. Phys.* **2015**, *87*, 1169–1181.

(20) Fu, B.; Flynn, J. D.; Isaacoff, B. P.; Rowland, D. J.; Biteen, J. S. Super-Resolving the Distance-Dependent Plasmon-Enhanced Fluorescence of Single Dye and Fluorescent Protein Molecules. *J. Phys. Chem. C* **2015**, *119*, 19350–19358.

(21) Lin, H.; Centeno, S. P.; Su, L.; Kenens, B.; Rocha, S.; Sliwa, M.; Hofkens, J.; Uji-i, H. Mapping of Surface-Enhanced Fluorescence on Metal Nanoparticles Using Super-Resolution Photoactivation Localization Microscopy. *ChemPhysChem* **2012**, *13*, 973–981.

(22) Willets, K. A. Super-Resolution Imaging of Interactions between Molecules and Plasmonic Nanostructures. *Phys. Chem. Chem. Phys.* **2013**, *15*, 5345–5354.

(23) Walhorn, V.; Paskarbeit, J.; Frey, H. G.; Harder, A.; Anselmetti, D. Distance Dependence of near-Field Fluorescence Enhancement and Quenching of Single Quantum Dots. *Beilstein J. Nanotechnol.* **2011**, *2*, 645–652.

(24) Wertz, E.; Isaacoff, B. P.; Flynn, J. D.; Biteen, J. S. Single-Molecule Super-Resolution Microscopy Reveals How Light Couples to a Plasmonic Nanoantenna on the Nanometer Scale. *Nano Lett.* **2015**, *15*, 2662–2670.

(25) Su, L.; Lu, G.; Kenens, B.; Rocha, S.; Fron, E.; Yuan, H.; Chen, C.; Van Dorpe, P.; Roeffaers, M. B. J.; Mizuno, H.; Hofkens, J.;

DOI: 10.1021/acsnano.6b03873
ACS Nano 2016, 10, 7955–7962

Hutchison, J. A.; Uji-i, H. Visualization of Molecular Fluorescence Point Spread Functions *Via* Remote Excitation Switching Fluorescence Microscopy. *Nat. Commun.* **2015**, *6*, 6287.
(26) Su, L.; Yuan, H.; Lu, G.; Rocha, S.; Orrit, M.; Hofkens, J.; Uji-i, H. Super-Resolution Localization and Defocused Fluorescence Microscopy on Resonantly Coupled Single-Molecule, Single-Nanorod Hybrids. *ACS Nano* **2016**, *10*, 2455−2466.
(27) Ropp, C.; Cummins, Z.; Nah, S.; Fourkas, J. T.; Shapiro, B.; Waks, E. Nanoscale Probing of Image-Dipole Interactions in a Metallic Nanostructure. *Nat. Commun.* **2015**, *6*, 6558.
(28) Nirmal, M.; Dabbousi, B. O.; Bawendi, M. G.; Macklin, J. J.; Trautman, J. K.; Harris, T. D.; Brus, L. E. Fluorescence Intermittency in Single Cadmium Selenide Nanocrystals. *Nature* **1996**, *383*, 802−804.
(29) Kuno, M.; Fromm, D. P.; Hamann, H. F.; Gallagher, A.; Nesbitt, D. J. Nonexponential "Blinking" Kinetics of Single CdSe Quantum Dots: A Universal Power Law Behavior. *J. Chem. Phys.* **2000**, *112*, 3117−3120.
(30) Kuno, M.; Fromm, D. P.; Hamann, H. F.; Gallagher, A.; Nesbitt, D. J. On"/"Off" Fluorescence Intermittency of Single Semiconductor Quantum Dots. *J. Chem. Phys.* **2001**, *115*, 1028−1040.
(31) Shimizu, K. T.; Neuhauser, R. G.; Leatherdale, C. A.; Empedocles, S. A.; Woo, W. K.; Bawendi, M. G. Blinking Statistics in Single Semiconductor Nanocrystal Quantum Dots. *Phys. Rev. B: Condens. Matter Mater. Phys.* **2001**, *63*, 205316.
(32) Bharadwaj, P.; Novotny, L. Robustness of Quantum Dot Power-Law Blinking. *Nano Lett.* **2011**, *11*, 2137−2141.
(33) Mertens, H.; Biteen, J. S.; Atwater, H. A.; Polman, A. Polarization-Selective Plasmon-Enhanced Silicon Quantum-Dot Luminescence. *Nano Lett.* **2006**, *6*, 2622−2625.
(34) Cheng, M.-T.; Liu, S.-D.; Wang, Q.-Q. Modulating Emission Polarization of Semiconductor Quantum Dots through Surface Plasmon of Metal Nanorod. *Appl. Phys. Lett.* **2008**, *92*, 162107.
(35) Maier, S. A. *Plasmonics: Fundamentals and Applications*, 1st ed.; Springer: New York, 2007; pp XXVI, 224.
(36) Tang, J.; Marcus, R. A. Mechanisms of Fluorescence Blinking in Semiconductor Nanocrystal Quantum Dots. *J. Chem. Phys.* **2005**, *123*, 054704.
(37) Frantsuzov, P.; Kuno, M.; Janko, B.; Marcus, R. A. Universal Emission Intermittency in Quantum Dots, Nanorods and Nanowires. *Nat. Phys.* **2008**, *4*, 519−522.
(38) Crouch, C. H.; Sauter, O.; Wu, X.; Purcell, R.; Querner, C.; Drndic, M.; Pelton, M. Facts and Artifacts in the Blinking Statistics of Semiconductor Nanocrystals. *Nano Lett.* **2010**, *10*, 1692−1698.
(39) Park, Y.-S.; Bae, W. K.; Padilha, L. A.; Pietryga, J. M.; Klimov, V. I. Effect of the Core/Shell Interface on Auger Recombination Evaluated by Single-Quantum-Dot Spectroscopy. *Nano Lett.* **2014**, *14*, 396−402.
(40) Bae, W. K.; Park, Y.-S.; Lim, J.; Lee, D.; Padilha, L. A.; McDaniel, H.; Robel, I.; Lee, C.; Pietryga, J. M.; Klimov, V. I. Controlling the Influence of Auger Recombination on the Performance of Quantum-Dot Light-Emitting Diodes. *Nat. Commun.* **2013**, DOI: 10.1038/ncomms3661.
(41) Peterson, J. J.; Nesbitt, D. J. Modified Power Law Behavior in Quantum Dot Blinking: A Novel Role for Biexcitons and Auger Ionization. *Nano Lett.* **2009**, *9*, 338−345.
(42) Tyagi, P.; Kambhampati, P. False Multiple Exciton Recombination and Multiple Exciton Generation Signals in Semiconductor Quantum Dots Arise from Surface Charge Trapping. *J. Chem. Phys.* **2011**, *134*, 094706.
(43) Park, S.-J.; Link, S.; Miller, W. L.; Gesquiere, A.; Barbara, P. F. Effect of Electric Field on the Photoluminescence Intensity of Single CdSe Nanocrystals. *Chem. Phys.* **2007**, *341*, 169−174.
(44) Houel, J.; Doan, Q. T.; Cajgfinger, T.; Ledoux, G.; Amans, D.; Aubret, A.; Dominjon, A.; Ferriol, S.; Barbier, R.; Nasilowski, M.; Lhuillier, E.; Dubertret, B.; Dujardin, C.; Kulzer, F. Autocorrelation Analysis for the Unbiased Determination of Power-Law Exponents in Single-Quantum-Dot Blinking. *ACS Nano* **2015**, *9*, 886−893.
(45) Pelton, M.; Smith, G.; Scherer, N. F.; Marcus, R. A. Evidence for a Diffusion-Controlled Mechanism for Fluorescence Blinking of Colloidal Quantum Dots. *Proc. Natl. Acad. Sci. U. S. A.* **2007**, *104*, 14249−14254.
(46) Verberk, R.; Orrit, M. Photon Statistics in the Fluorescence of Single Molecules and Nanocrystals: Correlation Functions *Versus* Distributions of On- and Off-Times. *J. Chem. Phys.* **2003**, *119*, 2214−2222.
(47) Lee, D.-H.; Yuan, C.-T.; Tachiya, M.; Tang, J. Influence of Bin Time and Excitation Intensity on Fluorescence Lifetime Distribution and Blinking Statistics of Single Quantum Dots. *Appl. Phys. Lett.* **2009**, *95*, 163101.
(48) Johnson, P. B.; Christy, R. W. Optical Constants of the Noble Metals. *Phys. Rev. B* **1972**, *6*, 4370−4379.
(49) Coomar, A.; Arntsen, C.; Lopata, K. A.; Pistinner, S.; Neuhauser, D. Near-Field: A Finite-Difference Time-Dependent Method for Simulation of Electrodynamics on Small Scales. *J. Chem. Phys.* **2011**, *135*, 084121.
(50) Brown, J.; Jull, E. V. The Prediction of Aerial Radiation Patterns from Near-Field Measurements. *Proc. Inst. Electr. Eng., Part B* **1961**, *108*, 635−644.
(51) Sun, Y.; Xia, Y. Large-Scale Synthesis of Uniform Silver Nanowires through a Soft, Self-Seeding, Polyol Process. *Adv. Mater.* **2002**, *14*, 833−837.

DOI: 10.1021/acsnano.6b03873
ACS Nano 2016, 10, 7955−7962